DOI: 10.13009/EUCASS2023-430
Aerospace Europe Conference 2023 – 10TH EUCASS – 9TH CEAS

Setup of a numerical methodology for the study of active-pressurization of cryogenic tanks

Francesca Rossetti[⋆†], *Marco Pizzarelli*[⋆⋆], *Rocco Pellegrini* [⋆⋆], *Enrico Cavallini* [⋆⋆], *and Matteo Bernardini* [⋆]
[⋆]*Sapienza University of Rome*
Via Eudossiana 18, 00184 Rome, Italy
[⋆⋆]*Italian Space Agency (ASI)*
Via del Politecnico s.n.c., Rome, 00133, Italy
f.rossetti@uniroma1.it · marco.pizzarelli@asi.it · rocco.pellegrini@asi.it · enrico.cavallini@asi.it · matteo.bernardini@uniroma1.it
[†]Corresponding author

Abstract

In this paper, a numerical methodology to study the active-pressurization inside cryogenic tanks is proposed and validated with the results of an active-pressurization experiment in normal gravity, inside a liquid nitrogen (N2) tank. The tank is modeled as 2D axisymmetric, a fluid-wall conjugate heat transfer model is used, and the two-phase fluid interface is tracked with the Volume-of-Fluid (VOF) method. The results show that the experimental data are accurately reproduced with the SST $k-\omega$ with low-Re corrections turbulence model, and that the modeling of the shutdown of pressurant gas injection requires some attention from a numerical standpoint.

1. Introduction

A cryogenic tank for a rocket or a satellite is actively pressurized by injecting a pressurant gas directly into the ullage, through the use of a diffuser. The pressurant gas can be of the same chemical species of the propellant already present in the tank or of another species, as in the very common case when the non-condensable helium (He) pressurant is used.

Active-pressurization is carried out in cryogenic tanks for aerospace applications for many reasons, among which to subcool the propellant in order to prevent boiling, to produce propellant expulsion during the engine burn, and to provide propellant to the turbopumps in proper pressure conditions such as to avoid cavitation.

Predicting the pressurant gas mass requirement is essential for the definition of cryogenic propulsion systems, and it is a challenging issue. Indeed, the pressurant gas mass requirement is influenced by many thermo-fluid-dynamics processes, among which the prevalent are associated with the heat transfer between the ullage and the tank wall and the heat and mass transfer between the ullage and the liquid.

Some previous experimental and numerical studies about active-pressurization in cryogenic tanks have been focused on the reduction of the pressurant gas requirement, for reasons of mass savings. These studies have revealed the influence of the following factors on the pressurant gas requirement: the inlet gas temperature [1, 2, 3, 4, 5], the diffuser design [1, 2, 5], the heat and mass transfer at the liquid-ullage interface [6], the pressurant gas species [7], and the tank wall thickness [5].

In the 1960s and 1970s, the first experimental studies of the active-pressurization phenomenon in cryogenic tanks in normal gravity were conducted at NASA. In particular, numerous experiments on tank pressurization during propellant expulsion were carried out [1, 2, 3, 4, 8, 9]. However, experiments of active-pressurization of cryogenic tanks without propellant expulsion can also be found in the literature [6, 10].

For the study of the active-pressurization inside cryogenic tanks, Computational fluid dynamics (CFD) offers many advantages over experimental studies, including the abolition of the costs associated with complex experiments and the speed up of the tank design. The literature regarding the numerical study of the active-pressurization is wide. In numerous studies, a numerical methodology is proposed and validated with experimental results. In particular, some of these studies are focused on tank pressurization without propellant expulsion [11, 12, 13], while, other studies analyze the problem of pressurization during propellant expulsion [5, 7, 14]. In some other CFD studies, operating conditions of interest are simulated. For example, the active-pressurization during atmospheric flight and the pressurized discharge

DOI: 10.13009/EUCASS2023-430

during the orbit flight, in a final stage liquid oxygen (O_2) tank, considering both aerodynamic heat and space solar radiation, were simulated in [15]. Later, the active-pressurization during the pre-launch phase, in the same tank and with the same propellant and pressurant gas as in [15], was simulated in [16]. In particular, the external forced convection heat exchange was taken into account, and the effect of different environmental temperatures was considered.
Another approach to simulate tank operations is the use of reduced order models, which allow to make quick estimates of the principal thermo-fluid-dynamics observables. Nevertheless, all the main physical phenomena involved in real systems can not be considered in a reduced order model, differently from CFD analyses. An example is the one-dimensional model, developed in [9], to simulate the problem of tank pressurization during propellant expulsion in a cylindrical tank. This model was validated against experimental results from [8] and [17], which were characterized by a variation of tank pressures, outlet flow rates, and pressurant gases.
The goal of this study is to define a numerical methodology able to describe the main thermo-fluid-dynamics phenomena occurring in an actively pressurized cryogenic tank, without propellant expulsion. Such a methodology guarantees to achieve accurate results both during and after the end of gas injection. Differently from previous studies, this study underscores why some modeling choices (for example a gradual termination of the pressurant gas injection) have a positive impact on the reliability of the results. The selected methodology is validated with the results of an active-pressurization experiment in normal gravity, inside a liquid N_2 tank [10]. The latter is pressurized through the injection, from a radial diffuser, of gaseous N_2, at a relatively high temperature. Therefore, the pressurant gas and the propellant are the same chemical species. The chosen validation test case has been selected for the accuracy of the initial and boundary conditions provided in [10].
This study is organized as follows. First, the main features of the physical-mathematical models are explained. Then, the chosen validation experiment is described. Next, the computational setup and the results of a grid convergence study are presented. Then, the problem of the uncertainty of the experimental data and of its influence on numerical results is discussed. Finally, a comparison is shown between the experimental results and the numerical ones obtained varying the numerical modeling of the pressurant gas injection.

2. Mathematical formulation

In this section, a brief description of the mathematical formulation used to model the active-pressurization inside cryogenic tanks is presented. In particular, the following parts are treated: the flow governing equations, the Volume-of-Fluid method, i.e. the method chosen for the liquid-ullage interface capturing, and the selected turbulence model.

2.1 Governing equations and thermophysical properties

The equations for conservation of mass, momentum, and energy are the following:

$$\frac{\partial \rho}{\partial t} + \nabla \cdot (\rho \boldsymbol{v}) = 0 \tag{1}$$

$$\frac{\partial}{\partial t}(\rho \boldsymbol{v}) + \nabla \cdot (\rho \boldsymbol{v}\boldsymbol{v}) = -\nabla p + \nabla \cdot \left[\mu_{eff}\left(\nabla \boldsymbol{v} + \nabla \boldsymbol{v}^T\right)\right] + \rho \boldsymbol{g} + \boldsymbol{F}_{vol} \tag{2}$$

$$\frac{\partial}{\partial t}(\rho E) + \nabla \cdot [\boldsymbol{v}(\rho E + p)] = \nabla \cdot \left(\lambda_{eff} \nabla T\right) + S_h \tag{3}$$

μ_{eff} and λ_{eff} are, respectively, the effective viscosity and the effective thermal conductivity, defined as the sum of the molecular contribution and of the possible turbulent contribution.
The Boussinesq approximation is used to model the density, ρ, of the liquid phase. With this approximation density is left constant in the governing equations, except in the buoyancy force term in the momentum equation (i.e., $\rho \boldsymbol{g}$), where density variation has a linear dependence on temperature. Constant thermophysical and transport properties, extracted from the National Institute of Standards and Technology (NIST) [18] database, at the average experimental temperature and pressure, have been used for the liquid N_2, as the latter is not subjected to large temperature variations throughout the experiment. Instead, temperature varying properties are used for both the gaseous N_2 and the wall, as they are both heated by several degrees, during the active-pressurization, due the injection of a relatively high temperature pressurant gas. In particular, for the gaseous N_2, density is modeled with the ideal gas equation of state, viscosity, μ, and thermal conductivity, λ, are modeled with Sutherland's law [19], and specific heat, c_p, is modeled with a piecewise linear approximation of the data taken from the NIST database, at the average experimental pressure. The selected wall material is, as stated in the experiment [10], stainless steel. Because the experimental data [10] lacked a specific description of the type of stainless steel, AISI 316 SS has been chosen, as it is sometimes used for cryogenic tanks.

DOI: 10.13009/EUCASS2023-430

However, if another type of stainless steel had been considered, the properties would have changed only slightly. A piecewise linear fit of the temperature dependent data taken from the NIST database [20] is used to model the wall specific heat and thermal conductivity. Instead, the wall density is modeled as constant, and equal to 8053.7 kg. All the liquid properties modeled as constant are listed in Table 1.

Table 1: Constant physical properties for the liquid N_2, taken from [18].

	ρ [kg/m^3]	λ [W/(m · K)]	c_p [J/(kg · K)]	μ [Pa · s]
Liquid N_2	804.14	0.144	2042.5	$1.579 \cdot 10^{-4}$

2.2 The Volume-of-Fluid method

The Volume-of-Fluid method [21] is one of the interface-capturing schemes, and it is based on the definition of the volume fraction, α, of a specific phase. The latter is zero if a cell is completely occupied by a specific phase, is one if it is completely occupied by the other phase, and is between zero and one for interface cells. When using the VOF method, an evolution equation for the volume fraction of the vapor, α_v, is added to the unique set of governing equations, Eqs. (1) - (3). This additional equation is used to track the interface between the liquid and vapor phases, and it is expressed as:

$$\frac{1}{\rho_v}\left[\frac{\partial}{\partial t}(\alpha_v \rho_v) + \nabla \cdot (\alpha_v \rho_v \boldsymbol{v}_v) = \dot{m}_{lv} - \dot{m}_{vl}\right] \tag{4}$$

The liquid volume fraction, α_l, can be computed using the constraint that the sum of the volume fractions of each phase must be equal to unity:

$$\sum_{q=l,v} \alpha_q = 1 \tag{5}$$

The phases volume fractions are, typically, used to define the average field variables and properties:

$$\rho = \sum_{q=l,v} \alpha_q \rho_q, \quad \mu_{eff} = \sum_{q=l,v} \alpha_q \mu_{eff_q}, \quad \lambda_{eff} = \sum_{q=l,v} \alpha_q \lambda_{eff_q} \tag{6}$$

The specific total energy, E, is defined as a mass averaged variable:

$$E = \frac{\sum_{q=1}^{2} \alpha_q \rho_q E_q}{\sum_{q=1}^{2} \alpha_q \rho_q} = \frac{\sum_{q=1}^{2} \alpha_q \rho_q e_q}{\sum_{q=1}^{2} \alpha_q \rho_q} + \frac{v^2}{2} \tag{7}$$

The two phases share the velocity field, v. The Lee model [22], which is a simplified saturation model used to calculate evaporation and condensation phase changes, is used to express the source terms in Eq. (4). In this model, the volumetric mass sources, $\dot{m}_{lv}$ and $\dot{m}_{vl}$, in [kg/(m^{3}s)], are driven by the difference between local temperature and saturation temperature:

$$\dot{m}_{lv} = r\alpha_l \rho_l \frac{T_l - T_{sat}}{T_{sat}} \qquad if \;\; T_l > T_{sat} \;\; (evaporation) \tag{8}$$

$$\dot{m}_{vl} = r\alpha_v \rho_v \frac{T_{sat} - T_v}{T_{sat}} \qquad if \;\; T_v < T_{sat} \;\; (condensation) \tag{9}$$

where r, in [1/s], is the mass transfer intensity factor, that is an empirical coefficient typically adjusted to have little discrepancies with the experimental data. r is the inverse of a relaxation time, and, theoretically, it should assume different values for evaporation and condensation. However, in this analysis, the same value of the mass transfer intensity factor has been used for both evaporation and condensation, as it has been done in some earlier numerical investigations [23, 24]. Being the difference between local temperature and saturation temperature the driving force for the phase change mass transfer, an accurate representation of the saturation line is fundamental for the precise calculation of the source terms in Eq. (4). In our simulations, the N_2 saturation line has been modeled with a piecewise linear fit of the values taken from the NIST [18] database. The source term S_h, in Eq. (3), is a volumetric heat source due to phase change, and is calculated through the product of the volumetric mass source by the latent heat of phase

DOI: 10.13009/EUCASS2023-430

change. The source term $\boldsymbol{F}_{vol}$, in Eq. (2), represents the contribution of surface tension force at the interface, which is modeled as a volumetric force, by means of the Continuum Surface Force (CSF) model [25, 26]. For constant surface tension, this term is expressed as:

$$\boldsymbol{F}_{vol} = \sigma_{lv} \frac{\rho \kappa_l \nabla \alpha_l}{\frac{1}{2}(\rho_l + \rho_v)} \tag{10}$$

where κ_l is the liquid surface curvature, defined as the divergence of the unit normal at the liquid interface:

$$\kappa_l = \nabla \cdot \hat{\boldsymbol{n}} \tag{11}$$

Finally, the gradient of the liquid volume fraction is used to determine the unit normal at the liquid interface:

$$\hat{\boldsymbol{n}} = \frac{\nabla \alpha_l}{|\nabla \alpha_l|} \tag{12}$$

2.3 Turbulence modeling

The maximum Rayleigh number, Ra, in the liquid phase, namely that just below the liquid-ullage interface, estimated using the numerical results, as its evaluation with the experimental data is unfeasible, is of the order of 10^{11}. So, it is much higher than the critical value for the transition from laminar to turbulent in a free convection boundary layer on a vertical plate, which is approximately equal to 10^9 [27]. Moreover, the Ra is above the critical value both during the active-pressurization phase and during the pressure decrease phase starting after the end of gas injection, where it is even higher, thus the fluid is expected to be in the turbulent regime during all the experimental duration.
In the following analyses, the SST $k-\omega$ with low-Re corrections turbulence model [28, 29] has been used. The SST $k-\omega$ model of Menter [28] brings together the benefits of the standard $k-\omega$ model of Wilcox [30] and of the $k-\varepsilon$ model. Moreover, it accounts for the transport of the turbulent shear stress in the definition of the turbulent viscosity. The low-Re corrections are included in the SST $k-\omega$ model to increment the accuracy in predicting low Reynolds number flows. Finally, when using the VOF model, a single set of transport equations for the turbulent quantities is solved for both phases, so that the turbulence variables have the same value for both phases throughout the field.

3. Computational setup

3.1 Test case description

The chosen validation experiment is an active-pressurization experiment, carried out in a liquid N_2 tank [10] in normal gravity. The test tank was enclosed in a vacuum casing, during the experiment, to better insulate it from the outside environment. The experiment was organized in two consequent phases. The first phase, which lasted for a time, t_{press}, of 60.7 s, was characterized by active-pressurization, during which a radial diffuser, placed at the top of the ullage, injected gaseous N_2, until the 300 kPa target pressure was obtained. The second phase, lasting 152.3 s, began when the tank inlet valve was closed. This phase was characterized by a pressure decrease, after which the pressure became constant, indicating the end of the experiment.
The test tank is cylindrical, with a round shaped bottom, as indicated in [10]. Figure 1 shows a tank scheme, together with the indication of the tank characteristic dimensions. The height of the liquid-ullage interface, H_l, is 0.445 m; the height of the ullage, H_v, is 0.205 m; and the tank inner radius, R, is 0.148 m. The tank's upper third has walls that are 1.5 mm thick, and its bottom third has walls that are 2 mm thick. After confirming, by means of earlier analyses, that employing a thickness, t_w, either of 1.5 mm or of 2 mm for the whole tank wall provides results that are about equivalent, in the numerical analysis the whole tank wall is modeled with a thickness of 2 mm. Moreover, the thickness of the lid, t_{lid}, is set at 6 mm, which is an approximate value, chosen after looking at a tank scheme in [10], as the precise value of the lid thickness was missing in [10].
The experiment's starting pressure is 104.2 kPa. Only evaporated N_2 is present in the tank ullage prior to pressurization starting. When the active-pressurization begins, a constant mass flow rate, equal to $8.3 \cdot 10^{-4}$ kg/s, of relatively hot gaseous N_2, with a temperature of 352 K, is injected. Numerous probes are used throughout the experiment to detect temperature, their positions are listed in Table 2, and are shown in Figure 1.

DOI: 10.13009/EUCASS2023-430

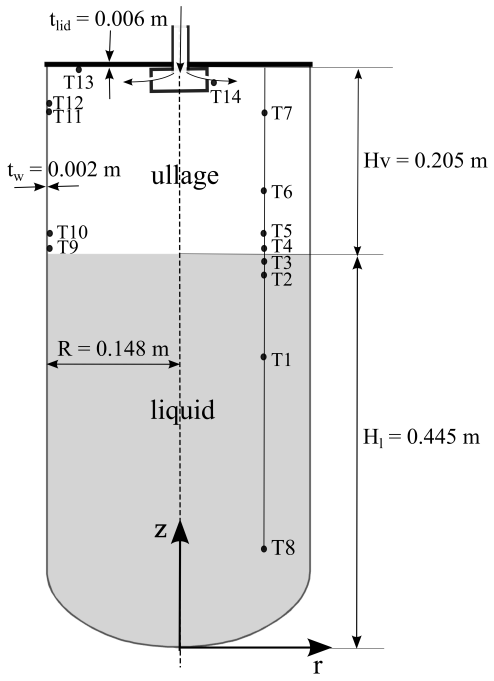

Figure 1: Tank scheme with the indication of the origin of the axisymmetric axes "r" and "z", of the tank characteristic dimensions, and of the position of the temperature probes (T1 to T14).

Table 2: Locations of the experimental temperature probes.

Probe	T1	T2	T3	T4	T5	T6	T7
r [m]	0.098	0.098	0.098	0.098	0.098	0.098	0.098
z [m]	0.33	0.43	0.44	0.45	0.46	0.51	0.61

Probe	T8	T9	T10	T11	T12	T13	T14
r [m]	0.098	-0.148	-0.148	-0.148	-0.148	-0.098	0.0063
z [m]	0.11	0.45	0.46	0.625	0.63	0.65	0.644

3.2 Flow solver

The pressure-based solver of the commercial CFD software Ansys Fluent [29] has been used to carry out transient analyses. The cylindrical geometry and the given boundary conditions allow to use the 2D axisymmetric model for the flow. A second order implicit time scheme is selected for time discretization. A time step of $1 \cdot 10^{-2}$ s has been chosen after preliminary convergence studies. A Courant number of 0.5 is used. A trade-off between computational cost and numerical accuracy has guided the choice of these parameters. The convective terms in density, momentum, energy, and turbulence equations are spatially discretized by means of second order upwind schemes, whilst, Ansys Fluent's "Compressive" scheme [29] is chosen for the volume fraction equation. "PRESTO!" scheme [29] is used to interpolate pressure values at the cell faces. The selected pressure-velocity coupling scheme is "Coupled" scheme [29].
Figure 2 schematizes the boundary conditions imposed in the simulations, which are the following: all the tank exterior surfaces, except the lid's ones, are set as adiabatic walls, indeed, they are subjected to a neglecting heat flux, due to the experiment's brief duration and to the insulation provided by the vacuum casing; the external surfaces of the lid are forced to be at a temperature of 280 K, as indicated in [10]; and the fluid-wall interfaces are set as no-slip coupled walls. Moreover, since the tank was equipped with a radial diffuser, a uniform and normal to the inlet surface mass flow rate, $\dot{m}_{pg}$, is imposed at the diffuser inlet surface during the active-pressurization phase. After that phase, an adiabatic wall boundary condition is imposed on that surface. The temperature of the pressurant gas is modeled as an interpolation of the gas temperature measured at the probe located immediately downstream of the diffuser. This probe is the T14, as indicated in Figure 1. It is worth noting that, the actual inlet gas temperature was lower than the one measured upstream

DOI: 10.13009/EUCASS2023-430

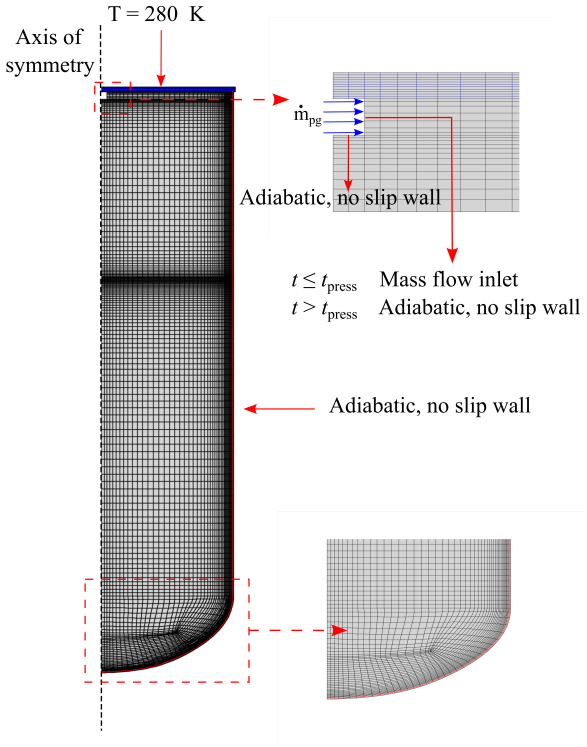

Figure 2: Selected computational grid (the domain has been modeled as 2D axisymmetric), with the indication of the boundary conditions used in simulations. Different colors are used for the fluid (grey), the wall (red), and the lid (blue) grids. In the right half of the figure, a zoom of the grid in proximity of the diffuser and a zoom of the grid in the round shaped bottom section of the tank are shown.

of the connecting pipe between the inlet valve and the diffuser (which was equal to 352 K).
The liquid and vapor phases are initialized as quiescent, at a pressure of 104.2 kPa. The liquid and the wall in contact with the liquid are initialized at a temperature of 77 K. A piecewise linear fit of the temperatures measured by the probes at the beginning of the experiment is used as the initial condition for the ullage and for the wall in contact with the ullage. Finally, the lid is initialized using a linear stratification between the temperatures of its lower surface and of its upper surface, which were 278 K and 280 K, respectively, as stated in [10].

3.3 Grid convergence study

A grid convergence study with four grids, characterized by an increasing level of spatial accuracy, has been carried out. The used grids are structured and their details, together with the time average of the percentage error, $E_{r\%}$, on pressure of the various grid levels, with reference to the finest grid, "Grid 4", are reported in Table 3.

Table 3: Details of the computational grids used for grid independence study.

	No. of cells [-]	**Wall-Interface spacing** [mm]	$E_{r\%}$ **w.r.t. Grid 4** [%]
Grid 1	2443	0.6	2.2
Grid 2	7690	0.6	2.5
Grid 3	31649	0.3	1.2
Grid 4	68294	0.2	[-]

Pressure evolutions obtained with the four grid levels are shown in Figure 3.
The grid levels from "Grid 2" to "Grid 4" are in the asymptotic range of convergence (being the average percentage error of "Grid 2" with respect to "Grid 3" of 1.3 % and the one of "Grid 3" with respect to "Grid 4" of 1.2 %). Instead, the coarsest grid, "Grid 1", produces results outside the range of asymptotic convergence, for this reason it has been discarded. As the results obtained with the "Grid 2" show a limited discrepancy with respect to the ones obtained with

DOI: 10.13009/EUCASS2023-430

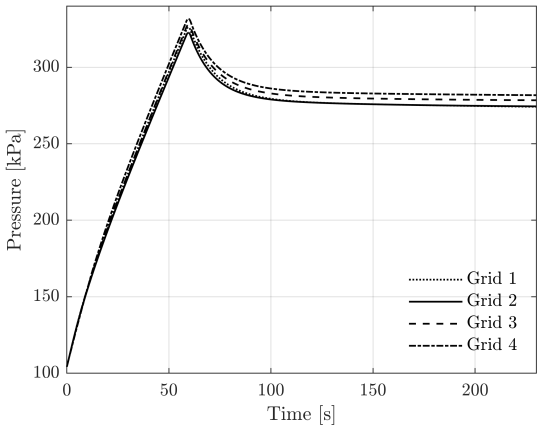

Figure 3: Numerical pressurization curves obtained with the four grids used for grid independence study. The characteristics of the used grids are summarized in Table 3.

the finest grid (the average percentage error between the two is of 2.5 %, as can be seen in Table 3), the "Grid 2" has been selected for subsequent analyses, in order to reduce the computational cost. The selected computational grid is represented in Figure 2. In the right half of the figure, a zoom of the grid in proximity of the diffuser and a zoom of the grid in the round shaped bottom section of the tank are shown, too. The characteristic average cell sizes of the "Grid 2" are of 4 mm and of 2 mm, in the fluid regions and in the wall region, respectively.

4. Results and discussion

4.1 The experimental uncertainty

An incongruity can be found when examining the experimental data at the initial time. Indeed, the initial ullage mass reported in [10] is practically equal to 0.035 kg, in contrast, it is equal to 0.0328 kg when computed using the experimental data at the initial time (pressure of 104.2 kPa, ullage volume, and temperature reconstructed with a piecewise linear fit of the initial measures of the temperature probes). This difference of about two grams influences the reproduction of the experimental pressurization rate, as it will be clear in the following. Therefore, the initial mass of the ullage has to be accurately quantified by experimental measures, in order to allow accurate CFD analyses. The inaccuracy in the computation of the initial vapor mass using the experimental data is caused by the uncertainty in the experimental measurements of pressure, temperature, and fill level, and it is not simple to comprehend how to change all these variables at once to recreate the original vapor mass mentioned in [10]. In this study, only the ullage volume has been changed in order to obtain the experimental initial ullage mass of 0.035 kg. In particular, the initial ullage volume, $V_u(0)$, has been incremented by 3.4 %, by increasing its height by 7 mm, from 0.205 m to 0.212 m.
Pressure evolutions obtained both with the nominal $V_u(0)$ and with the incremented $V_u(0)$ are shown in Figure 4, together with the corresponding experimental measures. The pressurant gas injection is more efficient (higher pressurization rate) when the ullage has a lower initial mass (case with the nominal $V_u(0)$), since active-pressurization is a quick and mostly mechanical process, that is only marginally affected by the heat transfer. The active-pressurization rate may be more accurately estimated when the incremented $V_u(0)$ is used, as a consequence, the match between experimental and numerical pressure evolutions is better also during the subsequent pressure decrease phase. For these reasons, the use of the incremented $V_u(0)$ has been retained in the subsequent part of the study.

4.2 Numerical modeling of the pressurant gas injection

During the first part of the experiment, namely the active-pressurization phase, the mass flow rate of the pressurant gas, $\dot{m}_{pg}$, is constant and equal to $8.3 \cdot 10^{-4}$ kg/s. When the gas injection is stopped, a second phase begins, which is characterized by pressure decrease. The modeling of the shutdown of the pressurant gas injection requires some attention from a numerical standpoint, to avoid having unphysical results. Indeed, if $\dot{m}_{pg}$ is instantaneously switched from its constant value to a zero value, an unphysical temperature decrease occurs in proximity of the diffuser and at the tank axis. This effect is apparent in Figure 5, showing temperature contours in the upper part of the tank, at two time instants, one just before the end of pressurant gas injection, precisely at 60 s, and the other just after the end of

DOI: 10.13009/EUCASS2023-430

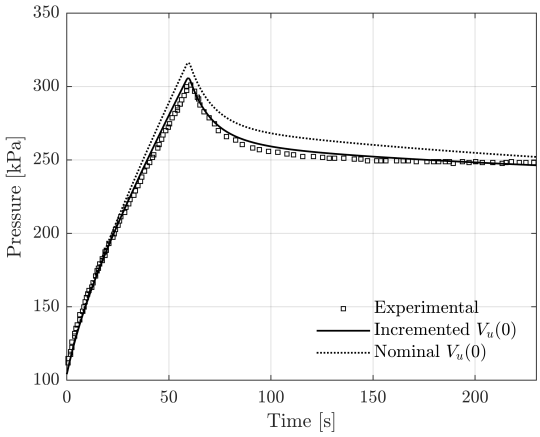

Figure 4: Comparison between experimental and numerical results of pressure evolution. Numerical predictions are presented both for the case with the nominal $V_u(0)$, from [10], and for the case with the $V_u(0)$ incremented by 3.4 %.

pressurant gas injection, precisely at 62 s. In particular, the figures on the left refer to the case in which the pressurant gas injection is stopped instantenously at 60.7 s, and the figures on the right refer to the case in which the pressurant gas injection shutdown is modeled with a linear decrease.

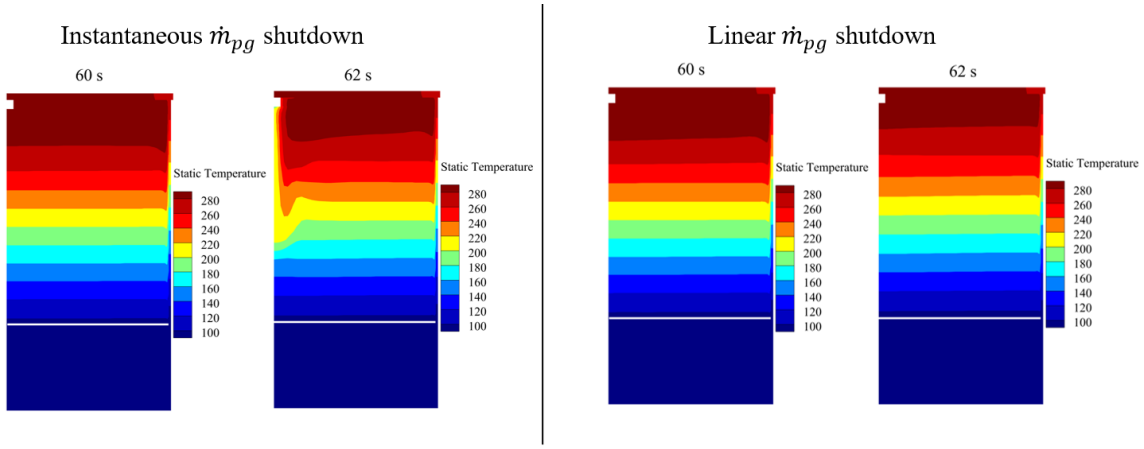

Figure 5: Temperature contours in the upper part of the tank, comprising the ullage and part of the liquid, at a time instant just before the end of pressurant gas injection, and at a time instant just after the end of pressurant gas injection. The figures on the left refer to the case in which the pressurant gas injection is stopped instantenously at 60.7 s, and the figures on the right refer to the case in which the pressurant gas injection shutdown is modeled with a linear decrease.

The latter modeling is more credible because, in the actual experiment, it is expected that the mass input does not cease immediately when the valve controlling the pressurant gas injection is closed. In the numerical analysis, this effect has been taken into account by modeling the pressurant gas mass flow rate with a profile characterized by the constant value of $8.44 \cdot 10^{-4}$ kg/s, in the first 58.7 s, and linearly decreasing to the value of zero, during the last two seconds of active-pressurization. The selected profile guarantees that the total pressurant gas mass injected into the tank remains equal to the experimental one. Nevertheless, the real valve shutdown behavior, which is not provided in [10], is approximated with this modeling.

If the pressure evolutions obtained using either a constant value for the mass flow rate, which is instantaneously stopped at 60.7 s, or the aforementioned profile are compared (see Figure 6), no relevant differences between them can be noticed. The only discrepancies are the slightly higher pressurization rate, the smoothing of the pressure peak (see the zoom in Figure 6 bottom right), and its slight anticipation, in the case when the profile for the pressurant gas mass flow rate is used. The use of the tested turbulence model, namely the SST $k - \omega$ with low-Re corrections, together with the selected more realistic model for the pressurant gas injection shutdown, allow to reproduce the experimental pressure evolution with high accuracy during both the active-pressurization phase and the pressure decrease phase. In

DOI: 10.13009/EUCASS2023-430

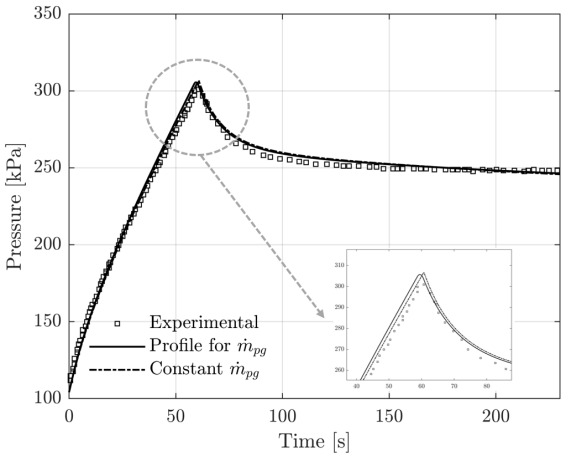

Figure 6: Comparison between experimental and numerical results of pressure evolution. A zoom of the pressure peak is shown in the bottom right corner of the figure. Numerical predictions have been obtained either by modeling the pressurant gas mass flow rate as constant, or by modeling it with a profile.

Figure 7, a comparison between experimental and numerical results of the ullage temperature at probe T14 (left) and ullage temperatures at probes T4, T5, T6, and T7 (right), is presented.

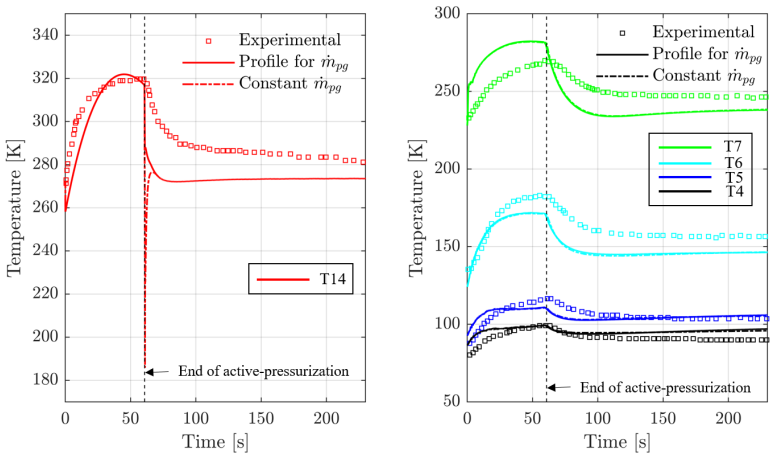

Figure 7: Comparison between experimental and numerical results of ullage temperature, at probe T14 (left) and ullage temperatures at probes T4, T5, T6, and T7 (right). Numerical results refer to simulations in which the pressurant gas mass flow rate is modeled either as constant, or with a profile.

The reader can refer to Table 2 and Figure 1 for details about the position of the experimental temperature probes. Numerical results refer to simulations in which the pressurant gas mass flow rate is modeled either as constant, or with a profile. Probe T14 is the one placed right downstream of the diffuser's inlet surface. A downward peak in the temporal evolution of the numerical temperature at probe T14 forms, at the conclusion of the active-pressurization phase, when the pressurant gas injection is halted instantly. Instead, the use of a smooth profile for the mass flow rate corrects this numerical effect. The remaining discrepancy between experimental and numerical T14 temperature values, even when using the smooth profile, can most likely be attributed to an approximate representation of the actual valve shutdown behavior. Moreover, the use of the profile for the pressurant gas mass flow rate corrects the aforementioned unphysical numerical effect, and does not alter the numerical temperature results from those obtained when the pressurant gas injection is arrested instantly. This is valid for both the ullage temperatures (see Figure 7) and the wall temperatures (see Figure 8 (left)), as well as for the liquid temperatures (see Figure 8 (right)). Both in the experiment and the simulations, the liquid bulk temperature is roughly constant and equal in the T1 and T8 probes. For this reason, the temperature at probe T8 has not been displayed for visual clarity. It is clear from Figures 7 and 8 that the numerical temperature profiles follow the experimental data with reasonable accuracy, with the the highest discrepancies found for the temperatures at the probe T3, which is the liquid probe closest to the interface and at the underlying probe T2.

DOI: 10.13009/EUCASS2023-430

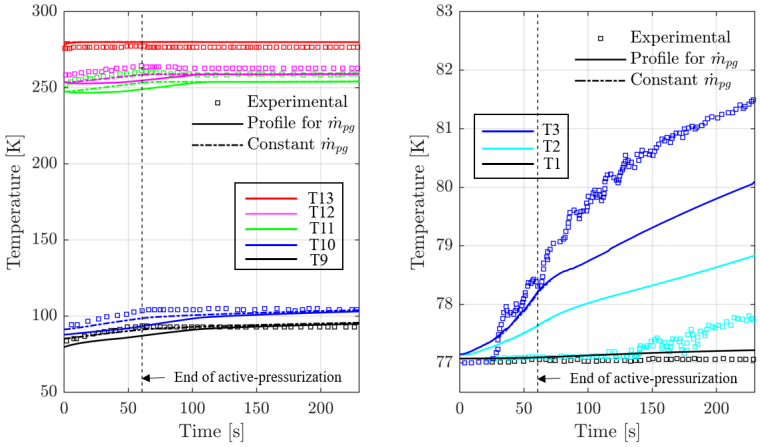

Figure 8: Comparison between experimental and numerical results of wall temperatures at probes T9, T10, T11, T12, and T13 (left) and liquid temperatures at probes T1, T2, and T3 (right). Numerical results refer to simulations in which the pressurant gas mass flow rate is modeled either as constant, or with a profile.

The phase change mass flow rate (see Figure 9), obtained as the volume integral of the source terms in Eq. 4, shows that both the models for the pressurant gas injection predict condensation during the whole experiment, apart from an evaporation spike in the initial instants. Indeed, from the right hand side of Eq. 4, it is visible that the phase change is positive if evaporation is greater than condensation, and negative otherwise. The obtained phase change result agrees with the analytical estimation made in [10], using the experimental data.

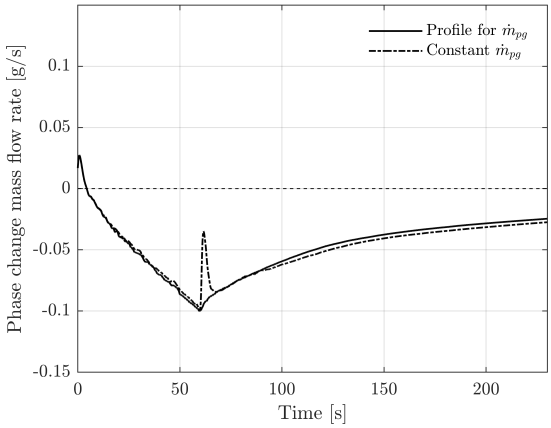

Figure 9: Phase change mass flow rate for the cases with the pressurant gas mass flow rate modeled either as constant, or with a profile.

Finally, it is apparent in Figure 9 that, in the case when the pressurant gas injection is stopped instantly, an unphysical spike forms in the phase change mass flow rate. This effect is again corrected with the use of a smooth profile for the mass flow rate.

5. Conclusions

In this study, a reliable numerical methodology to study the active-pressurization phenomenon is presented. It allows to have accurate results both during the pressurant gas injection phase and during the subsequent pressure decrease phase. This methodology has been selected comparing the numerical results with the data of an active-pressurization experiment in normal gravity, inside a liquid (N_2) tank [10]. Our numerical analyses have shown that:

- The initial ullage mass value affects the active-pressurization rate. Therefore, the numerical predictions are impacted by the experimental uncertainty of this parameter.

DOI: 10.13009/EUCASS2023-430

- To prevent getting unphysical outcomes, the numerical modeling of the final instants of the pressurant gas injection needs to be done carefully. In particular, unphysical temperature reductions and spikes of the phase change mass flow rate can be avoided by employing a decreasing profile for the pressurant gas mass flow rate, instead of halting it instantly at the end of the active-pressurization.
- The SST $k - \omega$ with low-Re corrections turbulence model allows to represent, with high accuracy, the experimental pressure evolution of the validation test case [10], both during the active-pressurization phase and during the pressure decrease phase.
- The SST $k - \omega$ with low-Re corrections turbulence model allows to reproduce the experimental temperature evolutions, measured by numerous probes located in the liquid, ullage and wall, with reasonable accuracy. The highest discrepancies between experimental and numerical data can be found for the liquid temperatures close to the liquid-ullage interface.

Even if the match between the experimental and numerical data is reasonably good, the proposed numerical methodology should be further refined and expanded through the testing of different turbulence models and of the laminar model, as well as with its validation with the results of other test cases having different operating conditions.

6. Acknowledgments

This research was jointly funded by Sapienza University and the Italian Space Agency - Agenzia Spaziale Italiana (ASI) as part of the research project: "Technical Assistance for launchers and propulsion" N.2019-4-HH.0 carried out under a framework research agreement CUP:F86C17000080005.

References

[1] R. J. Stochl, P. A. Masters, R. L. DeWitt, and J. E. Maloy. Gaseous hydrogen requirements for the discharge of liquid hydrogen from a 1.52-meter- (5-ft-) diameter spherical tank. *NASA Technical Note*, NASA TN D-5336, 1969.

[2] R. J. Stochl, P. A. Masters, R. L. DeWitt, and J. E. Maloy. Gaseous hydrogen requirements for the discharge of liquid hydrogen from a 3.96-meter- (13-ft-) diameter spherical tank. *NASA Technical Note*, NASA TN D-5387, 1969.

[3] R. J. Stochl, J. E. Maloy, P. A. Masters, and R. L. DeWitt. Gaseous-helium requirements for the discharge of liquid hydrogen from a 1.52 meter/5 ft/diameter spherical tank. *NASA Technical Note*, NASA TN D-5621, 1970.

[4] R. J. Stochl, J. E. Maloy, P. A. Masters, and R. L. DeWitt. Gaseous helium requirements for the discharge of liquid hydrogen from a 3.96 meter/13 ft/diameter spherical tank. *NASA Technical Note*, NASA TN D-7019, 1970.

[5] L. Wang, Y. Li, Z. Zhao, and J. Zheng. Numerical investigation of pressurization performance in cryogenic tank of new-style launch vehicle. *Asia-Pacific Journal of Chemical Engineering*, 9(1):63–74, 2014.

[6] W. A. Olsen. Experimental and analytical investigation of interfacial heat and mass transfer in a pressurized tank containing liquid hydrogen. *NASA Technical Note*, TN D-3219, 1966.

[7] L. Wang, Y. Li, C. Li, and Z. Zhao. CFD investigation of thermal and pressurization performance in LH2 tank during discharge. *Cryogenics*, 57:63–73, 2013.

[8] D. F. Gluck and J. F. Kline. Gas requirements in pressurized transfer of liquid hydrogen. Advances in Cryogenic Engineering: Proceedings of the 1961 Cryogenic Engineering Conference, University of Michigan Ann Arbor, Michigan, August 15–17, 1961, pages 219–233. Springer, 1962.

[9] W. H. Roudebush. An analysis of the problem of tank pressurization during outflow. *NASA Technical Note*, TN D-2585, 1965.

[10] C. Ludwig and M. E. Dreyer. Investigations on thermodynamic phenomena of the active-pressurization process of a cryogenic propellant tank. *Cryogenics*, 63:1–16, 2014.

[11] H. Scheufler and J. Gerstmann. Heat and mass transfer in a cryogenic tank in case of active-pressurization. *Cryogenics*, 121:103391, 2022.

DOI: 10.13009/EUCASS2023-430

[12] M.Stewart. Pressurization of a flightweight, liquid hydrogen tank: Evaporation & condensation at the liquid/vapor interface. 53rd AIAA/SAE/ASEE Joint Propulsion Conference, 2017.

[13] B. Ciccotosto and D. M. Hauser. Autogenous pressurization of a cryogenic tank using computational fluid dynamics. AIAA Propulsion and Energy 2021 Forum, 2021.

[14] L. Wang, Y. Li, Z. Zhao, and Z. Liu. Transient thermal and pressurization performance of LO2 tank during helium pressurization combined with outside aerodynamic heating. *International Journal of Heat and Mass Transfer*, 62:263–271, 2013.

[15] Z. Liu, Y. Li, and Y. Jin. Pressurization performance and temperature stratification in cryogenic final stage propellant tank. *Applied Thermal Engineering*, 106:211–220, 2016.

[16] Z. Liu, Y. Li, Y. Jin, and C. Li. Thermodynamic performance of pre-pressurization in a cryogenic tank. *Applied Thermal Engineering*, 112:801–810, 2017.

[17] Anon. Main propellant tank pressurization system study and test program. Prog. Rep. FTRL-TOR-61-23 (ER 5238), Lockheed-Georgia Co., 1961.

[18] E. W. Lemmon, M. O. McLinden, and D. G. Friend. Thermophysical properties of fluid systems. NIST Chemistry WebBook, NIST Standard Reference Database Number 69, Eds. Linstrom, P.J., and Mallard, W.G., National Institute of Standards and Technology, Gaithersburg MD, 20899, https://webbook.nist.gov.

[19] W. Sutherland. LII. the viscosity of gases and molecular force. *The London, Edinburgh, and Dublin Philosophical Magazine and Journal of Science*, 36(223):507–531, 1893.

[20] A. D. Keni and J. Taillon. Cryogenic material properties calculators. https://trc.nist.gov/cryogenics/calculators/propcalc.html, 2018. [Online; accessed July 2022].

[21] C.W. Hirt and B.D. Nichols. Volume of fluid (VOF) method for the dynamics of free boundaries. *Journal of Computational Physics*, 39(1):201–225, 1981.

[22] W. H. Lee. A pressure iteration scheme for two-phase flow modeling. *Computational Methods for Two-Phase Flow and Particle Transport*, pages 61–82, 2013.

[23] Z. Liu, Y. Li, and G. Zhou. Study on thermal stratification in liquid hydrogen tank under different gravity levels. *International Journal of Hydrogen Energy*, 43(19):9369–9378, 2018.

[24] Z. Liu, X. Yin, Y. Liu, Y. Li, and M. Andersson. Thermodynamic performance in a liquid oxygen tank during active-pressurization under different gas injection temperatures. *International Communications in Heat and Mass Transfer*, 140:106477, 2023.

[25] J.U Brackbill, D.B Kothe, and C. Zemach. A continuum method for modeling surface tension. *Journal of Computational Physics*, 100(2):335–354, 1992.

[26] C. R. Kharangate and I. Mudawar. Review of computational studies on boiling and condensation. *International Journal of Heat and Mass Transfer*, 108:1164–1196, 2017.

[27] F. P. Incropera, D. P. DeWitt, T. L. Bergman, and A. S. Lavine. *Fundamentals of heat and mass transfer*, volume 6. Wiley New York, 1996.

[28] F. R. Menter. Two-equation eddy-viscosity turbulence models for engineering applications. *AIAA journal*, 32(8):1598–1605, 1994.

[29] ANSYS fluent documentation. release 2022 R1. 2022.

[30] D. C. Wilcox. *Turbulence modeling for CFD*. DCW industries La Canada, CA, 1998.